

pubs.acs.org/acsaelm Article

Crystallization Behavior of Zinc-Doped Nb₂O₅ Thin Films Synthesized by Atomic Layer Deposition

Alexander C. Kozen, Jeffrey M. Woodward, Laura B. Ruppalt, Hans Cho, Carl A. Ventrice, Jr., Andrew H. Rowley, Nicole Zhe, Alex Mesiti, Emma Sargent, James H. Michels, and Zachary R. Robinson*



Cite This: ACS Appl. Electron. Mater. 2022, 4, 4280–4287



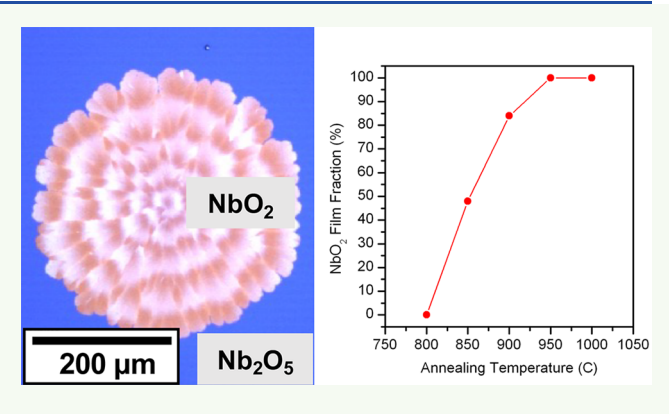
ACCESS

Metrics & More

Article Recommendations

Supporting Information

ABSTRACT: Neuromorphic computational devices built from memristive materials provide a potential path toward improved power and computational efficiency in a merged biomimetic and CMOS architecture. The key to such a framework is developing materials that can be reliably engineered into neuromorphic devices and integrated with CMOS platforms. Niobium dioxide has volatile memristive properties that make it an ideal candidate for future neuromorphic electronics. In this study, we thermally crystallized and reduced thin films of amorphous niobium oxide (Nb₂O₅) that were deposited with atomic layer deposition. We found that doping the as-deposited niobium oxide with zinc led to a lower initial crystallization temperature, which is a necessary step toward neuromorphic integration with CMOS devices that have a strict thermal budget.



KEYWORDS: neuromorphic, niobium oxide, atomic layer deposition, memristor, annealing, neuromorphic materials, thin films, XPS, CHESS

■ INTRODUCTION

With the end of the Moore's law era in sight, efforts to develop alternate approaches to improving computational capability have accelerated. Significant research has focused on braininspired "neuromorphic" approaches, which offer low-power stochastic device operation mimicking biological processes. One major circuit component of these neuromorphic approaches is the memristor, a resistor whose behavior is influenced by its previous state history. The first memristors leveraged oxygen-vacancy diffusion in slightly off-stoichiometric metal oxide thin films, predominantly TiO₂ and HfO₂, to achieve switching. As these devices show long relaxation lifetimes (on the order of months under ambient conditions), they are considered nonvolatile.

A second class of volatile memristors shows significantly shorter lifetimes. Typically, volatile memristors are fabricated using phase change materials (PCMs) like VO₂, whose conductivity can be modified by applying an external stimulus such as heat or pressure.³ When this external stimulus is removed, the material relaxes to its previous state, hence the volatility. Materials such as VO₂, for example, can exhibit up to a 4 order of magnitude change in conductivity due to the phase change. While there has been promising work using VO₂ as a phase change material, its low transition temperature (Tc) of

68 °C makes it susceptible to unintentional switching at operating circuit temperatures.

A promising analogue of VO_2 is NbO_2 , which also undergoes a structural phase transition that is accompanied by a large reduction in resistivity. NbO_2 undergoes a transition around 806 °C, which is expected to prevent unintentional switching due to elevated operated circuit temperatures but is still readily accessible in circuits using joule-heating resistive plugs. ^{4,5} The second-order phase transition is motivated by a change from a body-centered tetragonal (BCT) phase to a rutile phase. ^{5–8} This controllable, reversible change in electronic properties has made NbO_2 an attractive material for use in volatile memristors for low-power neuromorphic computing. ⁹

While NbO₂ thin films can be grown by a variety of methods, atomic layer deposition (ALD) of NbO₂ has several advantages for electronic devices, including the ability to deposit thin, conformal films on arbitrary 3D substrates at low

Received: April 21, 2022 Accepted: August 2, 2022 Published: August 11, 2022





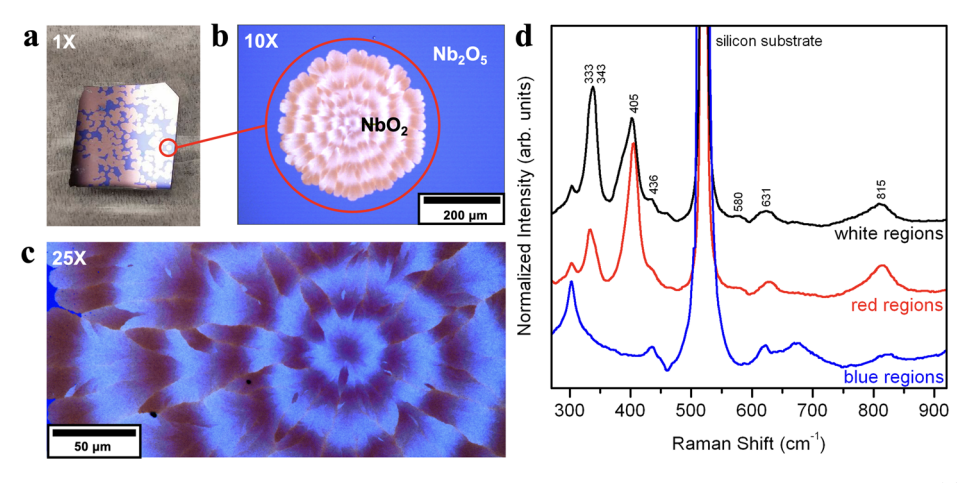


Figure 1. Optical microscopy images and Raman spectroscopy of an annealed Nb_2O_5 thin film grown on a Si wafer. Image (a) shows the entire 1×1 cm sample; (b) 10×1 image taken with an optical microscope; (c) 25×1 optical image of the annealed 10×1 NbO2 islands appear as red/white rings, and the 10×1 Substrate is uniformly blue; (d) Raman spectra of red (10×1 NbO2), white (10×1 NbO2), and blue (10×1 NbO2) regions. Additional spectra from Zn-doped 10×1 Raman spectra from Zn-doped 10×1

temperature and the ability to utilize digital doping techniques to deposit alloyed films by using alternating pulses of different chemical precursors. However, ALD films are typically amorphous and have a Nb₂O₅ stoichiometry. Producing crystalline NbO₂ from this material requires not only postdeposition crystallization but also postdeposition reduction, which we explore using a series of isothermal and isochronal anneals in forming gas at atmospheric pressure.

In this study, we show that \overline{ALD} -grown $\overline{Nb_2O_5}$ films can be both reduced and crystallized using a straightforward tube-furnace annealing process. We establish that atmospheric exposure of crystalline NbO_2 results in a native Nb_2O_5 oxide that is less than 2 nm thick. Finally, we show that incorporation of Zn dopants with ALD growth cycles of 1:10 Zn:Nb dramatically reduced both the temperature and time required for reduction and crystallization of the NbO_2 , without otherwise affecting the films.

■ EXPERIMENTAL SECTION

Amorphous $\mathrm{Nb_2O_5}$ films were deposited on (001) Si substrates in a Beneq TFS-200 ALD system using niobium-tert-butyltriethylamine (Nb-TBTEA) and water as reactants, with the reactor maintained at 200 °C for all growths. The Nb-TBTEA and $\mathrm{H_2O}$ precursors were maintained at 70 and 20 °C, respectively, with a saturative growth rate of 0.044 nm/cycle. The Nb-TBTEA pulses during film growth at appropriate pulse ratios of the constituent precursors to achieve the desired composition. For example, to achieve a 10% Zn:Nb2O5, we used a precursor pulse ratio of 1:10 DEZ:Nb-TBTEA. DEZ was maintained at 20 °C. All films used in this study were 65 nm thick as determined using spectroscopic ellipsometry (J.A. Woollam alpha SE using a Cauchy optical model).

Following NbOx deposition and diamond-scribe dicing (each sample was $\sim \! 1 \times 1$ cm), as-deposited samples were loaded into a quartz boat and placed in the center of an MTI GSL-1500X tube furnace. The samples were sealed in the furnace overnight at a pressure of 2 psig Ar. A forming gas mixture of 5% H_2 and 95% N_2 was introduced into the tube furnace at a rate of 60 sccm, and a needle valve on the exhaust was adjusted to maintain a sealed system pressure of $\sim \! 1.5$ psig during each anneal. Once the samples cooled to room temperature, the furnace was purged with argon, and the samples were removed.

Each sample was characterized with an Olympus BX51 microscope equipped with a color Infinity2-1RC digital camera. Color thresholding was performed with ImageJ, which took advantage of the fact

that the Nb_2O_5 changed from blue to red/white when it was reduced to NbO_2 .

The crystalline phase of each sample was determined with Raman spectroscopy. Custom Raman spectroscopy setups at the U.S. Naval Research Laboratory and the University of Rochester were used. In both systems, the samples were illuminated with a 532 nm laser, and the Raman scattered light was directed through a notch filter and into a monochromator.

The angle-resolved X-ray photoelectron spectroscopy (ARXPS) data were collected using a ThermoFisher Theta Probe XPS system. The system has a hemispherical electron energy analyzer with a position sensitive electron detector and a monochromated, microfocused Al–K α source. The X-ray beam diameter was set to 400 μm for each of the measurements presented in this study. The lens system and two-dimensional electron detector allow data to be collected simultaneously in 96 channels over a 60° range of photoelectron emission angles (23 to 83° with respect to the surface normal of the sample platen). For the ARXPS measurements, the 96 angle channels were binned into 8 angle channels, each with an angular acceptance of 7.5°. The angle-resolved spectra were acquired simultaneously at each analysis point while keeping the angle between the surface normal of the sample and the electron energy analyzer fixed at 53°.

The quantification of the area under each XPS peak was done using the Wagner library of photoionization cross sections. The secondary electron backgrounds were subtracted using a Smart fit, which is a Shirley background fit procedure that iteratively adjusts the background position so that it does not go above the data curve. The background subtraction and curve fitting of the data were done using the Avantage software package. A freshly cleaved HOPG sample was loaded onto the sample platen with the other samples, and the XPS measurement of the C-1s peak of the HOPG sample (284.50 eV) was used to calibrate the energy scale of the XPS system. For the overview spectra and the angle-resolved spectra, the pass energy of the analyzer was 100 eV. For the angle integrated spectra of the photoelectron core emissions, the pass energy of the analyzer was 20 eV.

Grazing incidence wide-angle X-ray scattering (GIWAXS) measurements were performed at the Cornell High Energy Synchrotron Source (CHESS) in beamline G2 and the National Synchrotron Light Source II (NSLS-II) on the Complex Materials Scattering (CMS) beamline. In GIWAXS experiments, an X-ray beam impinges upon a sample at a grazing angle and produces a scattering pattern, which is sensitive to features at interatomic and molecular length scales, thus providing a description of its crystalline structure. These patterns are collected by a 2D detector, and the coordinates of the intensity distribution are converted from pixel indices to momentum transfer Q for analysis. ¹⁴ The data was analyzed using a

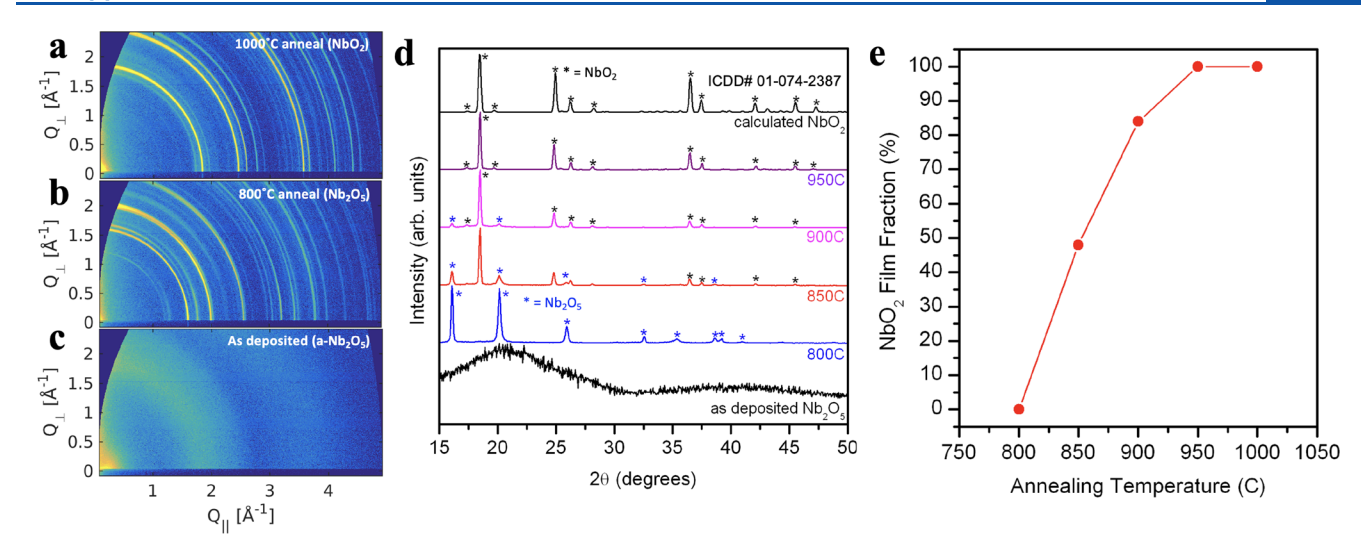


Figure 2. Reciprocal space maps of (a) ALD Nb_2O_5 annealed at 1000 °C for 1 h; (b) 800 °C for a 0 min hold time; (c) as-deposited Nb_2O_5 . Uniform diffraction lines indicate no preferred orientation to the crystals in annealed samples. (d) 1D XRD plots derived from a horizontal trace of the reciprocal space maps. (e) Calculated intensity ratio of the NbO_2 (400) diffraction line to the Nb_2O_5 (200) diffraction line, both the reference intensity peaks for the associated diffraction patterns.

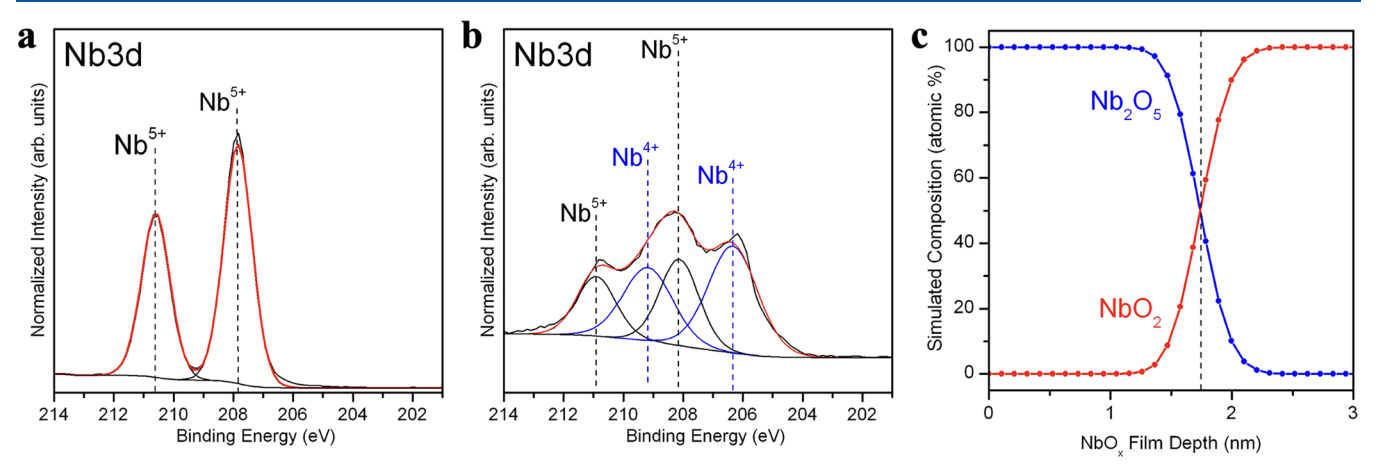


Figure 3. X-ray photoelectron spectroscopy from two different samples. Figure (a) is Nb 3d core levels from a sample annealed at 800 °C for 40 min. The presence of Nb in the 5+ oxidation state indicates Nb_2O_5 . Figures (b) and (c) were from a sample annealed at 975 °C for 40 min and show the presence of a ~1.6 nm surface oxide composed of Nb_2O_5 above a film of NbO_2 .

combination of the SciAnalysis package¹⁵ and custom Python and Matlab programs.

RESULTS AND DISCUSSION

Following anneals of the undoped samples, optical microscopy was performed, and images such as those in Figure 1b were taken. The images in Figure 1 were taken from a sample annealed at 850 °C. Two different regions can be seen in most of the samples, a homogeneous "blue" region with small islands that appear "red" and "white". Raman spectroscopy was used to determine the crystalline phase of the blue and red/white regions, respectively.

The Raman spectra for the sample in Figure 1a,b can be found in Figure 1d, which indicates that the red/white region is crystalline NbO₂. The peaks around 340, 405, 630, and 815 cm⁻¹ were used to identify NbO₂. Spectra taken from the uniform blue regions of the annealed samples reveal that it is crystalline Nb₂O₅. Raman spectra from as-grown samples were also measured (not shown) and confirm that, as-deposited, the films are amorphous. Transmission electron microscopy has confirmed these Raman results and are published elsewhere. ¹⁶

As-grown $\mathrm{Nb_2O_5}$ samples were annealed at a variety of temperatures and taken to CHESS for GIWAXS measurements. The spot size for this measurement is on the order of the sample size, owing to the glancing incidence. The full two-dimensional reciprocal space maps for samples annealed at 800 and 1000 °C for 20 min, along with an unannealed control sample, can be found in Figure 2a–c, respectively. Samples annealed at 850, 900, and 950 °C were also measured with GIWAXS, and representative 1D spectra from each sample are shown in Figure 2d, along with calculated spectra from the ICDD. The 1D spectra are linescans taken from the full reciprocal space maps.

The GIWAXS spectra of Figure 2 are consistent with Raman spectroscopy. Samples are fully amorphous as-grown, and crystallization as NbO_2 proceeds through an intermediate step of first crystallizing the Nb_2O_5 and then reducing into polycrystalline NbO_2 . The polycrystalline nature can be seen in the circular intensity rings in Figure 2a,b. Comparing the Nb_2O_5 and NbO_2 peak intensities gave us a straightforward way to determine the percentage of the surface recrystallized as NbO_2 , which is shown in Figure 2e. Figure 2e shows that

increasing the anneal temperature resulted in an increasing fraction of crystallized NbO $_2$, until the film is nearly completely crystallized and reduced at 950 °C. Both Raman and GIWAXS suggest that the color contrast indicates the crystalline state and provides a straightforward technique for using optical microscopy to study the crystallization kinetics.

In order to measure the sample stoichiometry and check for the presence of any impurities, X-ray photoelectron spectroscopy (XPS) was performed and is shown in Figure 3. The survey scans (not shown) show only the presence of niobium and oxygen, along with a small amount of adventitious carbon contamination. The spectra in Figure 3a are from a sample annealed at 800 °C, which appears uniformly blue in the optical microscope. The only peaks present near the Nb 3d energy range are in the 5+ oxidation state, indicating Nb₂O₅. For a sample annealed at 975 °C for 40 min, as in Figure 3b, the Nb 3d spectra show Nb in both the 5+ and 4+ oxidation states, which indicate the presence of both Nb₂O₅ and NbO₂. This sample was expected to be fully crystallized as NbO₂, based on both optical microscopy and Raman spectroscopy measurements.

An ARXPS measurement was taken, which allows inference of a depth profile by measuring the photoelectron kinetic energy as a function of the angle that the electron leaves the sample. This measurement confirmed that the Nb5+ peak in Figure 3b comes from the first 1.5 nm of the surface region, whereas the Nb4+ peak is from beneath the surface layer. Therefore, we conclude that the fully crystalline NbO₂ samples form a thin Nb₂O₅ surface oxide, likely due to exposure to atmospheric conditions and the increased stability in the atmosphere of Nb₂O₅. This native Nb₂O₅ layer that forms above the NbO₂, presumably upon atmospheric exposure, has been reported elsewhere. 5,6,16

In our initial attempts at creating crystalline thin films of NbO $_2$, samples were annealed for 20 min at a variety of temperatures, up to 1000 °C. Since the ultimate goal for memristive NbO $_2$ is incorporation in CMOS-compatible processes for merged architecture, we attempted to reduce the temperature needed for crystallization by incorporating Zn impurities in the Nb $_2$ O $_5$ ALD process.

Following synthesis of NbO $_x$ films with a 1:10 ratio of Zn:Nb ALD cycles, a series of anneals were performed, in which an undoped control sample and Zn-doped sample were placed in the tube furnace separated by about 1 cm. Anneals were performed at temperatures of 750, 825, 900, 975, and 1050 °C, each for times of 0 (furnace heated to the maximum temperature and then immediately cooled), 20, 40, and 60 min. The full temperature and time phase space were measured and characterized with optical microscopy. Similar measurements as those performed on the undoped NbO $_x$ samples were performed on a subset of the Zn-doped samples, which are summarized in Figure 4.

XPS measurements, shown in Figure 4a, were performed on the Zn-doped samples. A prominent Zn $2p_{3/2}$ peak can be seen around 1022 eV in the as-grown Zn-doped sample, which is shown in the bottom spectra. Based on the XPS peak intensity ratios, we expect the as-grown Zn-doped films to be ~8% Zn. However, this peak completely disappears following all of the anneals that we performed. These data imply that the Zn impurities added during film synthesis sublimate or dissolve into the bulk at elevated temperatures, although there may be a small concentration of Zn atoms left in the film that are below the measurement threshold for XPS.

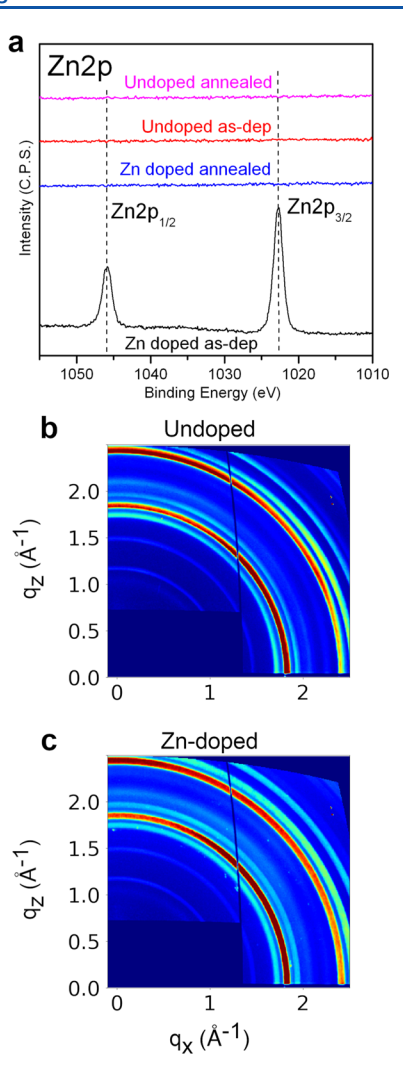


Figure 4. Summary of XPS and GIWAXS measurements on the Zn-doped samples. Plotted in (a) are four XPS spectra measured for the Zn-2p binding energy range. The annealing conditions are representative and were performed for 40 min at 975 °C. GIWAXS spectra for the annealed samples are shown in (b) and (c) for undoped and Zn-doped samples, respectively. Both spectra show polycrystalline NbO₂.

Raman spectroscopy and GIWAXS measurements were also performed on characteristic samples from the annealed Zndoped samples. The Raman spectra can be found in the Supporting Information, where it can be seen that both the Zndoped and undoped control sample both are crystalline NbO₂. Reciprocal space maps measured with GIWAXS at BNL for the undoped and Zn-doped samples are in Figure 4b,c, respectively. The spectra both indicate the presence of polycrystalline NbO2, with peaks at similar Q locations as Figure 2a. We note that generation of the more common intensity vs 2θ plot would be misleading in this case, due to the different incident X-ray beam energy and measurement geometry used at BNL compared to CHESS. These data reinforce the XPS measurements and imply that the addition of Zn to the NbOx growth process does not affect the postanneal chemical or structural state of the NbO₂ films.

For both the undoped and Zn-doped samples, optical images were taken at either 4× or 10× magnification, and the images were color-thresholded as in Figure 5. The optical thresholding was calibrated by first identifying the different

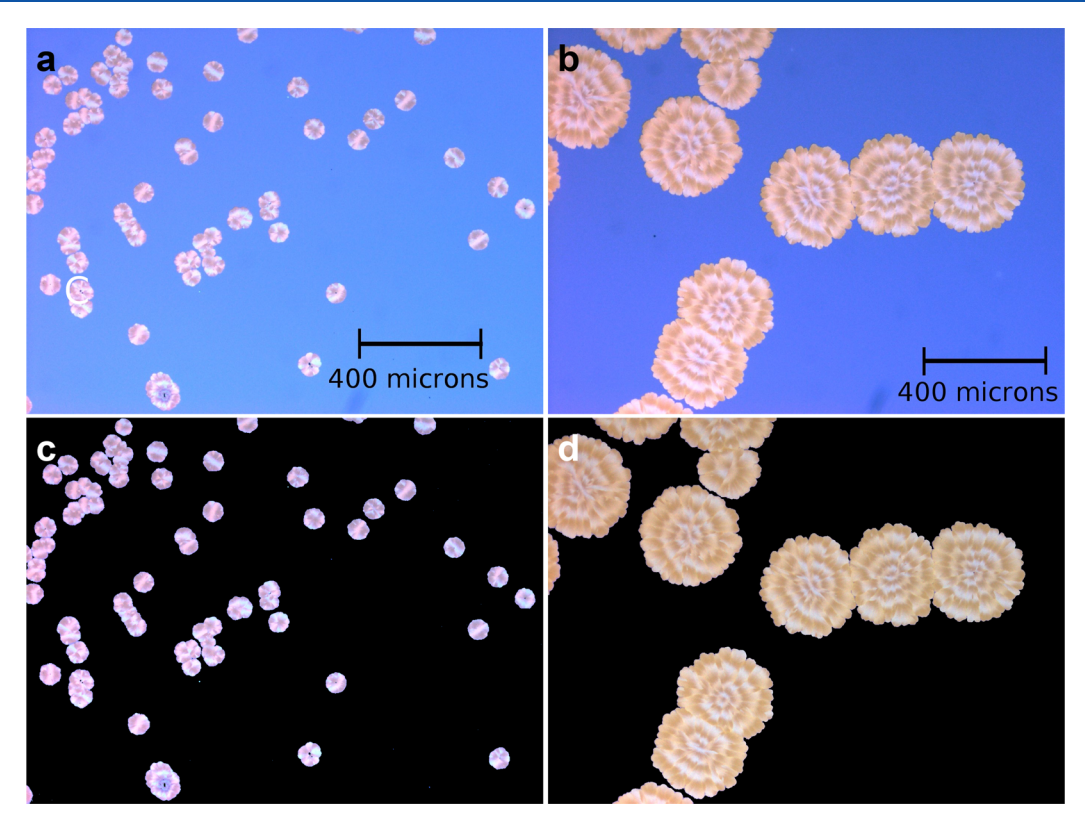


Figure 5. Optical microscopy images of undoped samples following two different anneals. The result of the ImageJ thresholding technique is shown in lower images. The image set in (a) and (c) was annealed at 800 °C for 20 min, and the images in (b) and (d) at 850 °C for 20 min.

phases using Raman spectroscopy. The color contrast that developed as a result of the changed phase (reduction from Nb₂O₅ to NbO₂) afforded us a straightforward technique for measuring the percentage of each sample that was converted to NbO₂. In Figure 5a,c, the Nb₂O₅ regions have been converted to black (pixel value 0), and then, the percentage of black pixels was calculated. The image used for Figure 5a,c was annealed at 800 °C for 20 min, and the images in Figure 5b, were annealed at 850 °C for 20 min. These optical measurements allowed us to collect a large number of sample statistics in a straightforward manner and map out the kinetics of the crystallization process.

All of the crystallization inferences, based on the optical images, are plotted in contour maps and shown in Figure 6. For anneals above 900 °C, both the undoped and Zn-doped samples fully recrystallized as NbO2, within the uncertainty of the optical technique, which we estimate to be around $\pm 0.5\%$. (The sample nonuniformity was considerably higher, as can be seen in Figure 1a. The 0.5% refers to the estimated uncertainty of the optical contrast technique itself.) However, the Zndoped samples showed significant crystallization as NbO2 at temperatures and for annealing times well below those observed in the undoped films. For instance, a 750 °C anneal performed for 60 min on an undoped, as-grown Nb₂O₅ sample showed that 21% of its surface had converted to crystalline NbO₂. A similar anneal—performed simultaneously—with the Zn-doped sample was 87% crystalline NbO₂. Similarly, the "0 min" anneal, in which the samples were heated to 825 °C and then immediately cooled (at 10 °C/min), resulted in 19% crystallization for the pristine Nb₂O₅ sample, whereas the Zndoped sample was 91% crystallized.

Anneals were also performed at 675 $^{\circ}$ C. XPS measurements indicated that the Zn had desorbed, but the samples appeared

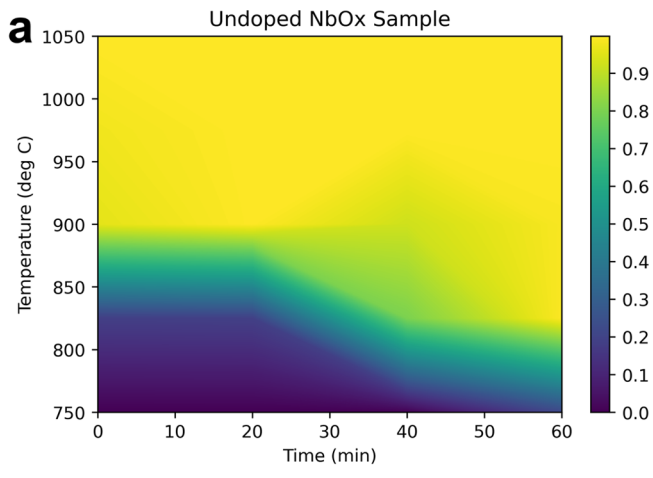
via Raman spectroscopy and optical microscopy to be fully amorphous. Therefore, we conclude that for the Zn-doped samples, crystallization occurs somewhere between 675 $^{\circ}\text{C}$ and 750 $^{\circ}\text{C}$.

Therefore, it appears that the addition of Zn in the growth process reduces the temperature required for crystallization, without having any effect on the crystallinity or purity of the NbO_2 film. We speculate that the vacancies created during Zn sublimation facilitate crystallization by increasing the driving force for the amorphous films to crystallize.

For many of the temperature and time annealing combinations, a detailed analysis of the crystallization kinetics is not possible because the samples were either fully crystallized for the shortest anneals or because full crystallization was not achieved even for long anneals. However, for the undoped samples annealed at 825 °C, the percentage of the surface that crystallized increases monotonically from 0 to 100% over the different anneal times (i.e., from 0 to 60 min anneals). Those data were analyzed using the Johnson-Mehl-Avrami-Kolmogorov (JMAK) model, 17-20 which has been noted to be applicable for 2D phase transitions for thin film growth on solid surfaces. 21-23 Those data were analyzed using the Avrami fitting technique, and the characteristic plots are shown in Figure 7. According to the JMAK model, isothermal crystallization (X) of the film is related to the annealing time (t) by the equation

$$X = 1 - e^{-mt^n} \tag{1}$$

where m and n are fitting parameters that are related to the kinetics of the crystallization process. The n fitting parameter has been shown to be related to the dimensionality of the growth, with modifications made to account for thin films. 19,24



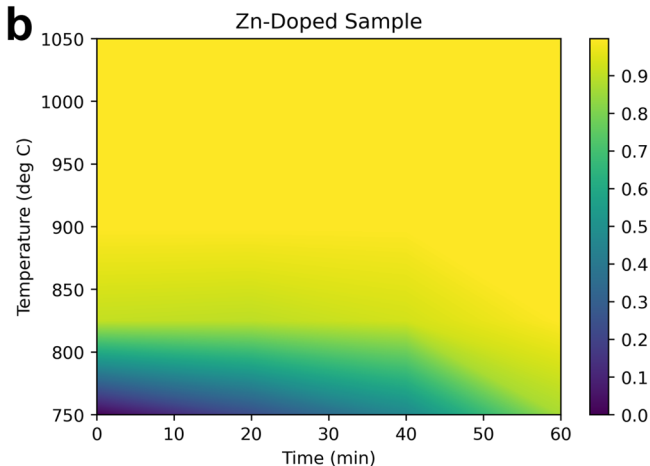


Figure 6. Contour plots, based on optical contrast analysis, mapping out the fraction of each sample that crystallized as NbO2 over the entire experimental parameter space of the tube furnace anneals. Plot (a) is for the undoped samples, and plot (b) is the Zn-doped.

Linearization of this equation, which is useful for fitting the model to our data, requires rearrangement and taking the natural log twice, which leads to the expression

$$\ln[-\ln(1 - X)] = \ln(m) + n\ln(t) \tag{2}$$

Our data along with the Avrami fits can be found in Figure 7, with the original model in Figure 7a and the linearized data (from which the fitting parameters were extracted) in 7b. Our n value, which is related to the dimensionality of the growth, is 2.86. Given the thin film nature of our samples, we presume that growth dimensionality transitions from a three-dimensional nucleation and initial growth, followed by a twodimensional growth once the crystalline islands reach the film thickness.23-

The m value of 4.4×10^{-5} is related to the nucleation and growth rate. When converted to units of 1/s, as in ref 24, our value of 30×10^{-3} 1/s is similar to values obtained for amorphous to crystalline transformation of TiO₂.

CONCLUSIONS

pubs.acs.org/acsaelm

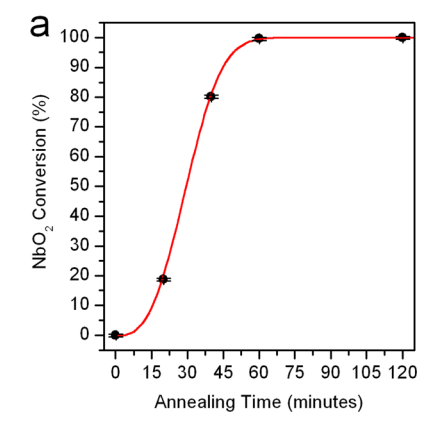
In order to use crystalline NbO2 or Nb2O5 in computational devices, control of the materials phase and crystallinity is required. While localized joule heating can crystallize Nb2O5 and NbO2 from amorphous constituent films, a reduction in required annealing temperatures would be desirable to reduce device power utilization and enable tighter integration with ondevice thermal budgets. Therefore, we studied the reduction and crystallization kinetics of amorphous, ALD Nb2O5, and Zn-doped Nb₂O₅. Nb₂O₅ was grown with Zn dopants in reasonably high concentrations, which resulted in an overall reduction in reduction/crystallization temperature. After annealing, no Zn was observed in the XPS spectra. We surmise that the vacancies in the film left by the sublimated Zn create a larger driving force for crystallization of the remaining niobium and oxygen atoms while leaving the film's structural and chemical properties unaffected.

ASSOCIATED CONTENT

Supporting Information

The Supporting Information is available free of charge at https://pubs.acs.org/doi/10.1021/acsaelm.2c00446.

Comparison of annealed fraction analysis between XRD and optical thresholding methods as well as Raman spectra of Zn-doped, undoped NbO2, and undoped Nb_2O_5 samples (PDF)



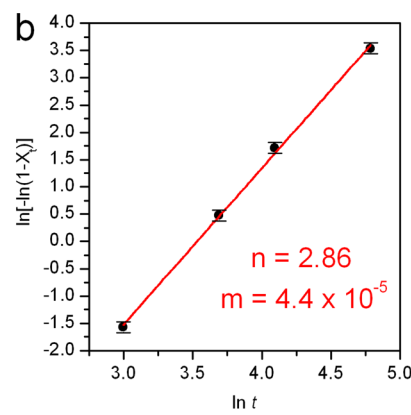


Figure 7. Avrami plot showing (a) the percent conversion of Nb₂O₅ to NbO₂ as a function of annealing hold time at 825 °C and (b) an Avrami plot with a linear fit to the data shown in (a). Error is estimated at 0.5% based on optical phase conversion analysis. The "n" and "m" fitting parameters are related to the dimensionality of the crystallization and the reaction rate kinetics, respectively.

AUTHOR INFORMATION

Corresponding Author

Zachary R. Robinson — Department of Physics, SUNY Brockport, Brockport, New York 14420, United States; orcid.org/0000-0002-1768-5988; Email: ZRobinson@ Brockport.edu

Authors

- Alexander C. Kozen Department of Materials Science & Engineering, University of Maryland, College Park, Maryland 20742, United States
- Jeffrey M. Woodward U.S. Naval Research Laboratory, Washington, DC 20375, United States
- Laura B. Ruppalt U.S. Naval Research Laboratory, Washington, DC 20375, United States
- Hans Cho U.S. Naval Research Laboratory, Washington, DC 20375, United States
- Carl A. Ventrice, Jr. College of Nanoscale Science and Engineering, SUNY Polytechnic Institute, Albany, New York 12203, United States
- Andrew H. Rowley Department of Physics, SUNY Brockport, Brockport, New York 14420, United States
- Nicole Zhe Department of Physics, SUNY Brockport, Brockport, New York 14420, United States
- Alex Mesiti Department of Physics, SUNY Brockport, Brockport, New York 14420, United States
- Emma Sargent Department of Physics, SUNY Brockport, Brockport, New York 14420, United States
- James H. Michels Department of Physics, SUNY Brockport, Brockport, New York 14420, United States

Complete contact information is available at: https://pubs.acs.org/10.1021/acsaelm.2c00446

Notes

The authors declare no competing financial interest.

ACKNOWLEDGMENTS

The authors from SUNY Brockport gratefully acknowledge support from NSF grant DMR-2103185. ACK acknowledges support from the ASEE. The authors would like to thank Professor Kathleen Dunn from SUNY Polytechnic for useful conversations about the crystallization process for Zn-doped samples. This research used the Complex Materials Scattering beamline of the National Synchrotron Light Source II, a U.S. Department of Energy (DOE) Office of Science User Facility operated for the DOE Office of Science by Brookhaven National Laboratory under Contract No. DE-SC0012704. The authors gratefully acknowledge Masafumi Fukuto and Ruipeng Li for their help in conducting the grazing incidence wideangle X-ray scattering experiments. This work is based upon research conducted at the Cornell High Energy Synchrotron Source (CHESS), which is supported by the National Science Foundation.

REFERENCES

- (1) Burkitt, A. N. A review of the integrate-and-fire neuron model: I. Homogeneous synaptic. *Biological cybernetics* **2006**, *95*, 1–19.
- (2) Strukov, D. B.; Snider, G. S.; Stewart, D. R.; Williams, R. S. The missing memristor found. *nature* **2008**, 453, 80–83.
- (3) Bae, S.-H.; Lee, S.; Koo, H.; Lin, L.; Jo, B. H.; Park, C.; Wang, Z. L. The memristive properties of a single VO2 nanowire with switching controlled by self-heating. *Adv. Mater.* **2013**, *25*, 5098–5103.

- (4) Funck, C.; Menzel, S.; Aslam, N.; Zhang, H.; Hardtdegen, A.; Waser, R.; Hoffmann-Eifert, S. Multidimensional simulation of threshold switching in NbO2 based on an electric field triggered thermal runaway model. *Advanced electronic materials* **2016**, *2*, 1600169
- (5) Wahila, M. J.; Paez, G.; Singh, C. N.; Regoutz, A.; Sallis, S.; Zuba, M. J.; Rana, J.; Tellekamp, M. B.; Boschker, J. E.; Markurt, T.; Swallow, J. E. N.; Jones, L. A. H.; Veal, T. D.; Yang, W.; Lee, T.-L.; Rodolakis, F.; Sadowski, J. T.; Prendergast, D.; Lee, W.-C.; Doolittle, W. A.; Piper, L. F. J. Evidence of a second-order Peierls-driven metalinsulator transition in crystalline NbO₂. *Phys. Rev. Materials* **2019**, *3*, 074602.
- (6) Páez Fajardo, G. J.; Howard, S. A.; Evlyukhin, E.; Wahila, M. J.; Mondal, W. R.; Zuba, M.; Boschker, J. E.; Paik, H.; Schlom, D. G.; Sadowski, J. T.; Tenney, S. A.; Reinhart, B.; Lee, W.-C.; Piper, L. F. J. Structural Phase Transitions of NbO2: Bulk versus Surface. *Chem. Mater.* **2021**, 33, 1416–1425.
- (7) O'Hara, A.; Demkov, A. A. Nature of the Metal-Insulator Transition in NbO2. *Phys. Rev. B* **2015**, *91*, 094305.
- (8) Eyert, V. The metal-insulator transition of NbO2: an embedded Peierls instability. EPL (Europhysics Letters) 2002, 58, 851.
- (9) Kumar, S.; Davila, N.; Wang, Z.; Huang, X.; Strachan, J. P.; Vine, D.; Kilcoyne, A. D.; Nishi, Y.; Williams, R. S. Spatially uniform resistance switching of low current, high endurance titanium-niobium-oxide memristors. *Nanoscale* **2017**, *9*, 1793–1798.
- (10) Hossain, N.; Günes, O.; Zhang, C.; Koughia, C.; Li, Y.; Wen, S.-J.; Wong, R.; Kasap, S.; Yang, Q. Structural and physical properties of NbO2 and Nb2O5 thin films prepared by magnetron sputtering. *J Mater Sci: Mater Electron* **2019**, *30*, 9822–9835.
- (11) Kozen, A. C.; Robinson, Z. R.; Glaser, E. R.; Twigg, M.; Larrabee, T. J.; Cho, H.; Prokes, S. M.; Ruppalt, L. B. In Situ Hydrogen Plasma Exposure for Varying the Stoichiometry of Atomic Layer Deposited Niobium Oxide Films for Use in Neuromorphic Computing Applications. ACS Appl. Mater. Interfaces 2020, 12, 16639–16647.
- (12) Park, N.; Kim, Y. T.; Park, Y.; Cho, J. Y.; Oh, S. S.; Heo, J.; Son, J. Voltage-triggered insulator-to-metal transition of ALD NbO x thin films for a two-terminal thresholdswitch. *Journal of Materials Chemistry C* **2020**, *8*, 14365–14369.
- (13) Park, Y.; Yoon, D.; Fukutani, K.; Stania, R.; Son, J. Steep-slope threshold switch enabled by pulsed-laser-induced phase transformation. ACS Appl. Mater. Interfaces 2019, 11, 24221–24229.
- (14) Renaud, G.; Lazzari, R.; Leroy, F. Probing surface and interface morphology with grazing incidence small angle X-ray scattering. *Surf. Sci. Rep.* **2009**, *64*, 255–380.
- (15) Yager, K. G. https://github.com/CFN-softbio/SciAnalysis.
- (16) Twigg, M.; Kozen, A.; Ruppalt, L.; Prokes, S.; Cho, H. Transmission electron microscopy analysis of reduction reactions and phase transformations in Nb2O5 films deposited by atomic layer deposition. *J. Appl. Phys.* **2021**, *129*, 025304.
- (17) Avrami, M. Kinetics of phase change. I General theory. *J. Chem. Phys.* **1939**, *7*, 1103–1112.
- (18) Avrami, M. Kinetics of phase change. II transformation-time relations for random distribution of nuclei. *J. Chem. Phys.* **1940**, *8*, 212–224
- (19) Burke, J.; Turnbull, D. Recrystallization and grain growth. *Progress in metal physics* **1952**, *3*, 220–292.
- (20) Kolmogorov, A. N. On the statistical theory of the crystallization of metals. *Bull. Acad. Sci. USSR, Math.Ser.* **1937**, *1*, 355–359.
- (21) Fanfoni, M.; Tomellini, M. The johnson-mehl-avrami-kohnogorov model: a brief review. *Il Nuovo Cimento D* **1998**, 20, 1171–1182.
- (22) Holloway, P.; Hudson, J. Kinetics of the reaction of oxygen with clean nickel single crystal surfaces: I. Ni (100) surface. *Surf. Sci.* **1974**, *43*, 123–140.

- (23) Moghadam, M.; Voorhees, P. W. Thin film phase transformation kinetics: From theory to experiment. *Scripta Materialia* **2016**, 124, 164–168.
- (24) Ağırseven, O.; Biswas, P.; Tate, J. Amorphous-to-crystalline transition of thin-film TiO2 precursor films to brookite, anatase, and rutile polymorphs. *J. Mater. Res.* **2022**, *37*, 1135–1143.
- (25) Pang, E.; Vo, N.; Philippe, T.; Voorhees, P. Modeling interface-controlled phase transformation kinetics in thin films. *J. Appl. Phys.* **2015**, *117*, 175304.

□ Recommended by ACS

Anionic Flow Valve Across Oxide Heterointerfaces by Remote Electron Doping

Yunkyu Park, Junwoo Son, et al.

NOVEMBER 17, 2022 NANO LETTERS

READ 🗹

A Digital-Analog Integrated Memristor Based on a ZnO NPs/CuO NWs Heterostructure for Neuromorphic Computing

Yaqi Wang, Yang Li, et al.

JUNE 24, 2022

ACS APPLIED ELECTRONIC MATERIALS

READ 🗹

Reduction of Twin Boundary in NbN Films Grown on Annealed AlN

Shunya Kihira, Hiroshi Fujioka, et al.

JANUARY 11, 2022

CRYSTAL GROWTH & DESIGN

READ 🗹

Electron Doping-Induced Metal–Insulator Transition in LaNiO $_3$ and Memory Devices

Qi Wang, Shriram Ramanathan, et al.

APRIL 29, 2022

ACS APPLIED ELECTRONIC MATERIALS

READ 🗹

Get More Suggestions >